



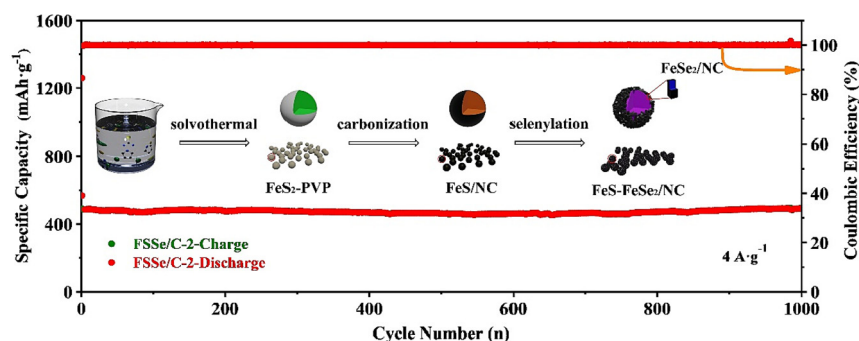
# Bonding iron chalcogenides in a hierarchical structure for high-stability sodium storage



Hongyi Chen, Pengfei Lv, Qiming Liu<sup>\*</sup>, Pengfu Tian, Shiyue Cao, Shengjun Yuan

Key Laboratory of Artificial Micro- and Nano-structures of Ministry of Education, School of Physics and Technology, Wuhan University, Wuhan 430072, China

## GRAPHICAL ABSTRACT



## ARTICLE INFO

### Article history:

Received 3 December 2022

Revised 10 January 2023

Accepted 11 January 2023

Available online 13 January 2023

### Keywords:

Sodium ion batteries  
Hierarchical architecture  
Heterogeneous interfaces  
Synergistic effect

## ABSTRACT

Owing to price-boom and low-reserve of Lithium ion batteries (LIBs), cost-cutting and well-stocked sodium ion batteries (SIBs) attract a lot of attention, aiming to develop an effective energy storage and conversion equipment. As a typical anode for SIBs, Iron sulfide (FeS) is difficult to maintain the high theoretical capacity. Structural instability and inherent low conductivity limit the cyclic and rate performance of FeS. Herein, hierarchical architecture of FeS-FeSe<sub>2</sub> coated with nitrogen-doped carbon (NC) is obtained by single-step solvothermal method and two-stage high-temperature treatments. Specifically, lattice imperfections provided by heterogeneous interfaces increase the Na<sup>+</sup> storage sites and fasten ion/electron transfer. Synergistic effect induced by the hierarchical architecture effectively enhances the electrochemical activity and reduces the resistance, which contributes to the transfer kinetics of Na<sup>+</sup>. In addition, the phenomenon that heterogeneous interfaces provide more active site and extra migration Na<sup>+</sup> path is also proved by density functional theory (DFT). As an anode for SIBs, FeS-FeSe<sub>2</sub>/NC (FSSe/C) delivers highly reversible capacity (704.5 mAh·g<sup>-1</sup> after 120 cycles at 0.2 A·g<sup>-1</sup>), excellent rate performance (326.3 mAh·g<sup>-1</sup> at 12 A·g<sup>-1</sup>) and long-lasting durability (492.3 mAh·g<sup>-1</sup> after 1000 cycles at 4 A·g<sup>-1</sup> with 100 % capacity retention). Notably, the full battery, assembled with FSSe/C and Na<sub>3</sub>V<sub>2</sub>(PO<sub>4</sub>)<sub>3</sub>/C (NVP/C), delivers reversible capacity of 252.1 mAh·g<sup>-1</sup> after 300 cycles at 1 A·g<sup>-1</sup>. This work provides a facile method to construct a hierarchical architecture anode for high-performance SIBs.

© 2023 Elsevier Inc. All rights reserved.

## 1. Introduction

Currently, with the increasingly heavy ecological environment problems, new energy has been evolved as a valuable alternative to fossil energy [1–4]. Developing efficient energy storage and con-

<sup>\*</sup> Corresponding author.

E-mail address: [qmliu@whu.edu.cn](mailto:qmliu@whu.edu.cn) (Q. Liu).

version equipment is an urgent need for new energy resources. Lithium ion batteries (LIBs) are known for low weight, high energy density and fast charging [5–8]. However, the shortage and the single distribution of lithium (Li) source cannot meet the growing demand for power equipment, which limits the further development of LIBs [9]. Sodium source is low-cost (\$ 150 t<sup>-1</sup>), widely distributed ( $23.6 \times 10^3$  mg·kg<sup>-1</sup>) and readily available. Furthermore, Sodium ion batteries (SIBs) and LIBs have the same “rocking chair” principle of charge/discharge, which makes SIBs a reasonable alternative to LIBs [10,11]. Nevertheless, the larger radius and heavier mass of Na<sup>+</sup> than Li<sup>+</sup> cause greater structural damage in the active electrode during the cyclic process [12]. Therefore, it is crucial to synthesize suitable electrode materials for SIBs.

Owing to the open-frame architectures, high theoretical capacity and low cost, transitional metal chalcogenides (TMCs) have been proved as a potential anode material for SIBs [13–15]. Iron sulfide (FeS) as a typical TMCs has advantages of high theoretical specific capacity (609 mAh·g<sup>-1</sup>), well-stocked, cost-cutting and non-pollution [16–18]. Unfortunately, high expansion rate affects the stability and low electrical conductivity leads to the poor rate capacity of converted-type electrode of FeS [19,20]. Many strategies, such as designing hierarchical structure [9,21], adjusting window voltage [10,22] and using carbon-coating [23–25], have been employed to validly solve these stubborn problems.

It has been proved that the capacity and stability of FeS can be increased by constructing a hierarchical architecture. Phase boundaries of different components provide abundant point, line and planar defects, which increase more active site for storage of Na<sup>+</sup> and improve the charge transfer by enhancing reaction kinetics [26,27]. In addition, the synergistic effect of heterogeneous parts reduces the accumulation of nanocrystals in the intermediate process, restraining the capacity attenuation during the cyclic process [28]. Yang et al. designed a composite structure of MoO<sub>2</sub>/MoS<sub>2</sub>/NC that delivers the reversible capacity of 419.8 mAh·g<sup>-1</sup> [29]. Dong et al. synthesized Sb/ZnS/C with the hierarchical architecture, which achieves the capacity of 554.8 mAh·g<sup>-1</sup> at 0.1 A·g<sup>-1</sup> after 150 cycles [30]. Li et al. obtained CoP/C-FeP anode and it can retained 456.2 mAh·g<sup>-1</sup> at 0.1 A·g<sup>-1</sup> after 200 cycles [31]. Nevertheless, the long-period capability of the electrode at high current density remains to be improved.

Herein, the spherical precursor of FeS/NC (FS/C) is synthesized by a single hydrothermal and subsequent carbonization treatment. After the selenization, FeSe<sub>2</sub> nanorods grow on the surface of FS/C that builds the hierarchical architecture of FeS-FeSe<sub>2</sub>/NC (FSSe/C). The 2D FeSe<sub>2</sub> nanorods reduce the diffusion path of Na<sup>+</sup> and improve the charge transfer dynamics. The lattice imperfections originating from the phase boundary provide abundant reactive sites for storage of Na<sup>+</sup> and enhance the electron/ion transfer capability. In addition, nitrogen doped carbon (NC), converted from polyvinyl pyrrolidone (PVP), is coated on the surface of FeS-FeSe<sub>2</sub>, which is beneficial to slowing down the structural damage and inhibiting the shuttle effect. In addition, density functional theory (DFT) calculation also proves that FeS/FeSe<sub>2</sub> interfaces can provide the adsorption site and reduce the adsorption energy of Na<sup>+</sup>. FSSe/C as an anode for SIBs delivers reversible capacity (704.5 mAh·g<sup>-1</sup> after 120 cycles at 0.2 A·g<sup>-1</sup>) and superior rate performance (326.3 mAh·g<sup>-1</sup> at 12 A·g<sup>-1</sup>). FSSe/C keeps reverse capacity of 492.3 mAh·g<sup>-1</sup> after 1000 cycles even at the high current density of 4 A·g<sup>-1</sup>. Moreover, the full battery, assembled with FSSe/C and Na<sub>3</sub>V<sub>2</sub>(PO<sub>4</sub>)<sub>3</sub>/C (NVP/C), delivers reversible capacity of 252.1 mAh·g<sup>-1</sup> after 300 cycles at 1 A·g<sup>-1</sup>. The excellent electrochemical properties demonstrate the potential of FSSe/C as an electrode material for SIBs.

## 2. Experimental

Ethylene glycol (99.5 %), FeSO<sub>4</sub>·7H<sub>2</sub>O (99 %), polyvinyl pyrrolidone (PVP, 99 %), thiourea, sulfur powder (S, 99.5 %) and selenium powder (Se, 99 %) were purchased from Aladdin. None of the reagents were further purified.

### 2.1. Preparation of FeS<sub>2</sub>/PVP

Typically, 1.112 g FeSO<sub>4</sub>·7H<sub>2</sub>O was grinded to powder and dissolved in 50 mL ethylene glycol. Then, 0.8 g PVP was dispersed into the mixture. After stirring at room temperature for 30 min, 0.304 g thiourea and 0.192 g sulfur powder were added to the above mixture and ultra-sounded for 20 min. The mixed solution was transferred into 80 mL Teflon stainless steel autoclave and placed in the oven at temperature of 180 °C for 18 h. After repeated washing and centrifuging, the product was dried overnight in a vacuum.

### 2.2. Preparation of FeS/NC (FS/C)

Typically, 200 mg of FeS<sub>2</sub>/PVP was laid flat on the porcelain boat. Then, the porcelain boat was put in a furnace (Argon atmosphere) and annealed at 600 °C for 3 h.

### 2.3. Preparation of FeS-FeSe<sub>2</sub>/NC (FSSe/C)

Typically, 60 mg FS/C and 20/40/60 mg Se were mixed evenly and placed into a porcelain boat. The porcelain boat was put in a furnace (Argon atmosphere) and heated at 300 °C for 4 h. Then the temperature was risen to 400 °C at the ramp rate of 5 °C·min<sup>-1</sup> and kept for 1.5 h to remove redundant Se. Samples added with 20, 40 and 60 mg Se were named FSSe/C-1, FSSe/C-2 and FSSe/C-3, respectively.

### 2.4. Preparation of Na<sub>3</sub>V<sub>2</sub>(PO<sub>4</sub>)<sub>3</sub>/C cathode (NVP/C)

Na<sub>3</sub>V<sub>2</sub>(PO<sub>4</sub>)<sub>3</sub>/C cathode material was obtained by the way we did it before [32].

### 2.5. Characterization of materials

X-ray diffractometer (XRD, Bruker D8 advance, Cu K $\alpha$  radiation,  $\lambda = 1.5406$  Å) pattern was employed to analyze the formation process and phase composition. The composition of samples and valence state were tested by X-ray photoelectron spectroscopy (XPS, Al K $\alpha$  radiation, USA). Field emission scanning electron microscope (Zeiss GeminiSEM 500) and transmission electron microscopy (TEM, JEM-2010 HT and JEM-F200) were used to examine the morphology and lattice spacing. N<sub>2</sub> adsorption apparatus (JW-BK100B) was employed to measure the Brunauer Emmett and Teller (BET) surface area.

### 2.6. Electrochemical measurements

First, the homogeneous slurry is composed of active materials, carbon, carboxymethyl cellulose (CMC) and polymerized styrene butadiene rubber (SBR) in a ratio of 6:2:1:1. Copper foil with uniformly slurry-coating is used as the collecting and dried in an oven with vacuum environment (current collector utilizes aluminum foil only when the cathode is NVP/C). Second, dried copper foil is cut into 12 mm discs and the load of active substance on each disc is between 1.2 and 1.5 mg·cm<sup>-2</sup>. Last, all the discs were employed to fabricate the 2032-type coin cells, and the corresponding coun-

ter electrode is metallic sodium or NVP/C. Glass fiber filter and sodium trifluoromethanesulfonate ( $\text{NaCF}_3\text{SO}_3$ ) in diglyme (DGM) were used as the separator and electrolyte, respectively. Electrochemical performance was examined by land battery testing system (LANHE-CT2001). Electrochemical impedance spectroscopy (EIS) and cyclic voltammogram (CV) were tested on electrochemical workstation.

### 2.7. Theoretical Calculations/Computational detail/Calculation methods

The first-principles calculations were performed by using the projector augmented wave (PAW) [33] method as implemented in the Vienna Ab initio Simulation Package (VASP) [34] code. Generalized gradient approximation (GGA) in the form of Perdew-Burke-Ernzerhof (PBE) [33] was used as the exchange–correlation functional. The vdW-DF3 functional [35] which was proven to be a good description of weak van der Waals interactions was also taken into account. The energy cut-off for plane-wave expansion and the width of smearing were set as 500 eV and 0.05 eV, respectively.

For the calculations of the interface energy, the Monkhorst–Pack [36] scheme k-point grid of  $(1 \times 1 \times 1)$  was used for relaxation and a grid of  $(3 \times 3 \times 3)$  was used for self-consistent field calculations until the change of total energy is less than  $10^{-5}$  eV. A vacuum layer of 15 Å in thickness was introduced for the interface in z direction to avoid spurious interactions.

For the single  $\text{Na}^+$  diffusion barrier energy calculations and associated minimum energy pathways, climbing image-nudged elastic band method (CI-NEB) [37] was employed.

## 3. Results and discussion

As shown in Fig. 1,  $\text{FeS}_2$ -PVP was prepared by a single-step hydrothermal method. In the subsequent annealing process at 600 °C,  $\text{FeS}_2$  was desulfurized to FeS (hexagonal phase), and PVP was carbonized to NC. In the selenylation process, the surface of FeS/NC reacted with the molten selenium powder to form  $\text{FeSe}_2$  at 300 °C, and the internal hexagonal-FeS (H-FeS) was affected by orthorhombic- $\text{FeSe}_2$  to form orthorhombic-FeS (O-FeS).

X-ray diffractometer (XRD) pattern was employed to analyze the formation process and phase composition of FSSe/C. As shown in Fig. 2a, the substance synthesized in the solvent-thermal method is  $\text{FeS}_2$ -PVP (PDF#71-0053, cubic phase). During the subsequent carbonized process at 600 °C,  $\text{FeS}_2$  changes into FeS (PDF#75-0602, hexagonal phase) and the excess S-atoms are lost in the form of S vapor. In addition, polyvinyl pyrrolidone (PVP) is decomposed into nitrogen-doped carbon (NC) in the process of carbonization. In the following high temperature reaction (Fig. 2c), atomic substitution between S and Se leads to the formation of  $\text{FeSe}_2$  (PDF#21-0432, orthorhombic phase) at 300 °C (the melting temperature of Se is 217 °C). In particular, the internal FeS do not transform to  $\text{FeSe}_2$ , but it changed from hexagonal to

orthorhombic system ( $\text{FeS}$ , PDF#76-0964, orthorhombic phase) due to the influence of external orthorhombic  $\text{FeSe}_2$ . When Se is insufficient, relatively small amounts of  $\text{FeSe}_2$  have little effect on hexagonal-FeS, so the hexagonal-FeS and orthorhombic-FeS can be detected in Fig. 2b. When Se is in excess (Fig. 2d), the existing phase of FSSe/C-3 is consistent with FSSe/C-2. The whole process of formation of FSSe/C-2 can be simplified as follows: 1.  $\text{FeS}_2$ -PVP is synthesized by the hydrothermal process; 2.  $\text{FeS}_2$ -PVP is transformed to (hexagonal-FeS)/NC; 3. (hexagonal-FeS)/NC is transformed to (orthorhombic-FeS)- $\text{FeSe}_2$ /NC.

The composition of FSSe/C-2 and valence state were measured by X-ray photoelectron spectroscopy (XPS). As shown in Fig. 3a, elemental signals including Fe, S, Se, C and N can be detected in FSSe/C-2. Fe 2p high-resolution spectrum (Fig. 3b) can be separated into two peaks at 707.3 (Fe  $2p_{3/2}$ ) and 720.1 eV (Fe  $2p_{1/2}$ ), associated with theoretical valence of Fe in FSSe/C-2 [38,39]. In the S 2p (Fig. 3c) spectrum, there are five main peaks located at 160.8, 162.1, 163.6, 166.1 and 168.6 eV, associating with Fe-S and surficial oxidation [2,9]. As shown in Fig. 3d, the main peaks appear at the binding energy of at 54.5 and 55.5 eV, which corresponds to the iron selenide [40–42]. In the C 1s high-resolution spectrum (Fig. 3e), the peaks located at 284.6 and 285.7 can be attributed to with C–C and C–N chemical bonds, respectively [43–45]. The presence of carbon slows the volume expansion during the process of charging/discharging. As shown in N 2p spectrum (Fig. 3f), the peaks at 399.3 and 400.2 eV are contributed to pyridinic and pyrrolic N. And N-doped C can further improve the conductivity of the carbon [9,46] (see Fig. 4).

The morphology of FSSe/C with hierarchical architecture was determined by field emission scanning electron microscope (SEM) and transmission electron microscopy (TEM). The SEM and TEM images (Fig. 4a–c) shows that FS/C microspheres have a relatively smooth surface with an average diameter of 2.5 μm. The SEM and TEM images of FSSe/C-2 are depicted in Fig. 4d, e and f. After the selenization process,  $\text{FeSe}_2$  is formed by atomic substitution between the molten Se powder and FeS.  $\text{FeSe}_2$  crystal are grown on the surface of FS/C to form  $\text{FeSe}_2$  nanorods. Two-dimensional nanorods with a length of about 200 nm and a width of about 40 nm shorten the migration distance of  $\text{Na}^+$  and improve the reaction dynamics. NC (amorphous) also exists in the outer layer of nanorods, which protects the material structure from destruction (Fig. 4g). The high-resolution TEM (HRTEM) image (Fig. 4h) shows two regions with different types of lattices spacing. By measuring the lattice spacing of the Fourier transform (Fig. 4i), region 1 is consisted of two interlaced lattice fringes, corresponding to (121) crystal face of FeS and (010) of  $\text{FeSe}_2$ . Region 2 only contains one lattice fringe, originating from (121) crystal face of FeS (Fig. 4j). Notably there is a distinct phase interface between regions 1 and 2, which provides more lattice mismatches, distortions, and defects for storage of  $\text{Na}^+$  and improves charge transfer by enhancing the reaction dynamics. Meanwhile, the element distribution is shown in Fig. 4k, which delivers the homogeneous distribution of Fe, S, Se, C, and N-atoms in the composite.

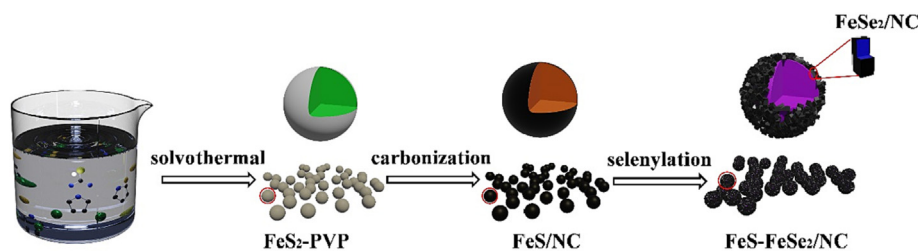


Fig. 1. Schematic diagram of formation of FSSe/C.

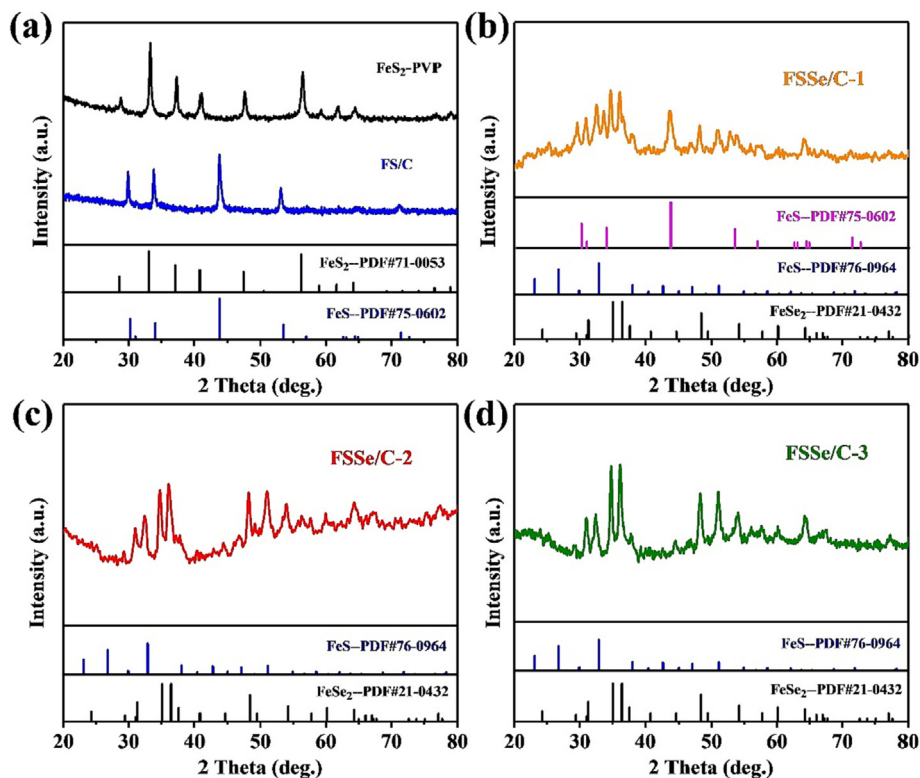


Fig. 2. The XRD patterns of (a)  $\text{FeS}_2$ -PVP, FS/CN, (b) FSSe/C-1, (c) FSSe/C-2 and (d) FSSe/C-3.

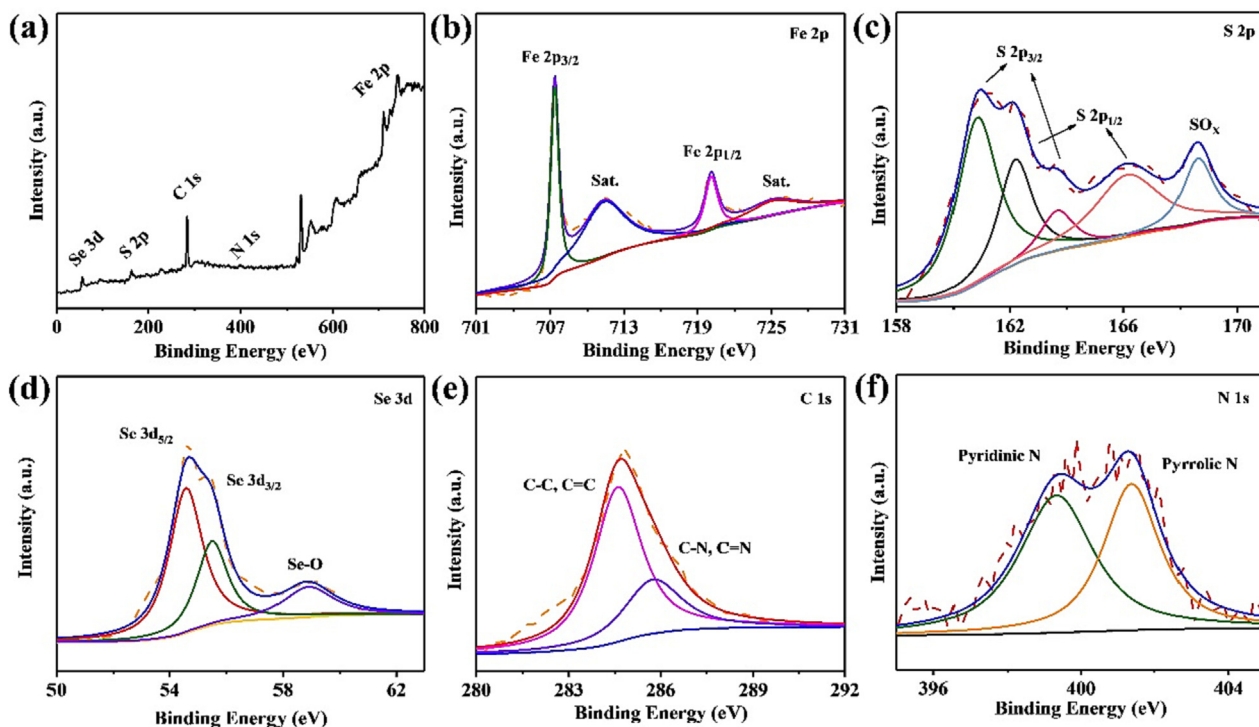
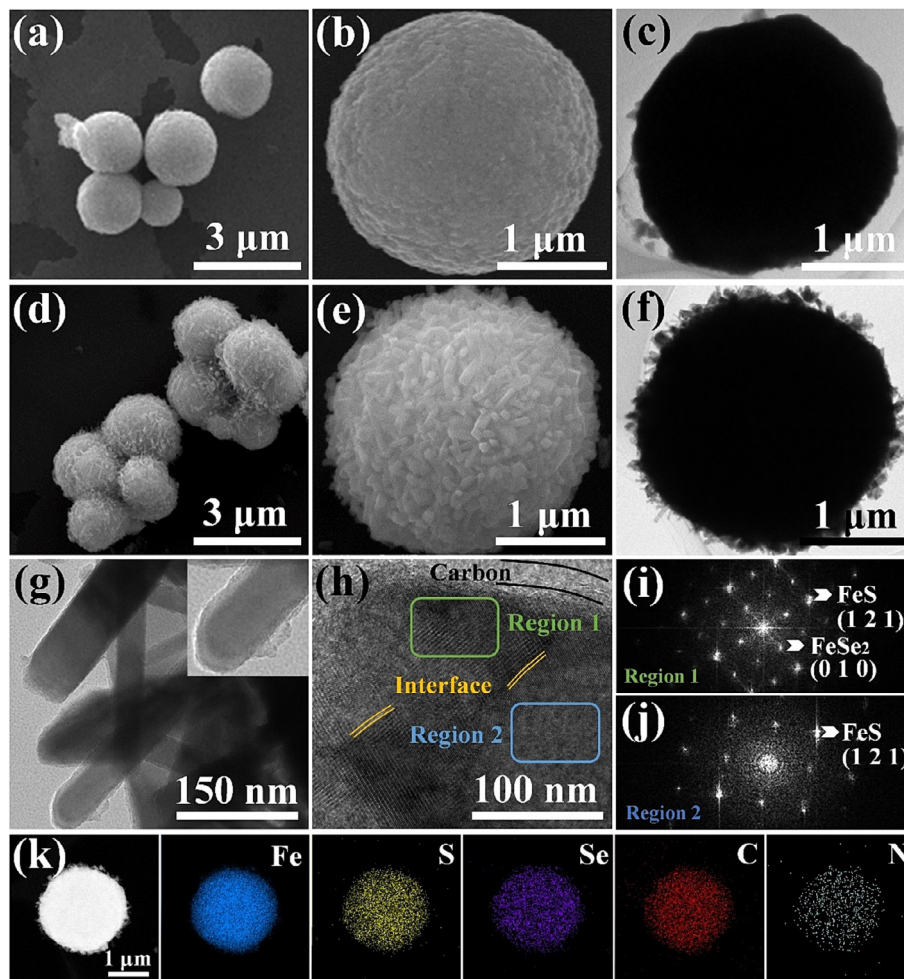


Fig. 3. (a) XPS spectra of survey spectrum. XPS spectra of (b) Fe, (c) S, (d) Se, (e) C and (f) N for FSSe/C-2.

More TEM and HRTEM images of FSSe/C-2 are shown in Fig. 5a-d. As displayed in Fig. 5a, the distinct hierarchical architecture of FeS,  $\text{FeSe}_2$  and NC provides a large number of phase boundaries. Abundant lattice mismatches, distortions and defects affect the storage of  $\text{Na}^+$  and transport of charge carrier by adjusting long-

range disorder. According to the measurement of the regional Fourier (Fig. 5b), the nanorods grown during the selenization are single crystal of  $\text{FeSe}_2$ . As displayed in Fig. 5c-d, a large number of FeS- $\text{FeSe}_2$  phase interfaces provides more active sites to store  $\text{Na}^+$ . Fig. 5e-f and g-h show the TEM images of FSSe/C-1 and



**Fig. 4.** (a, b) SEM and (c) TEM images of FS/C. (d, e) SEM and (f, g) TEM images of FSSe/C-2. (h) HRTEM, (i, j) region Fourier transform and (k) elemental mapping images of FSSe/C-2.

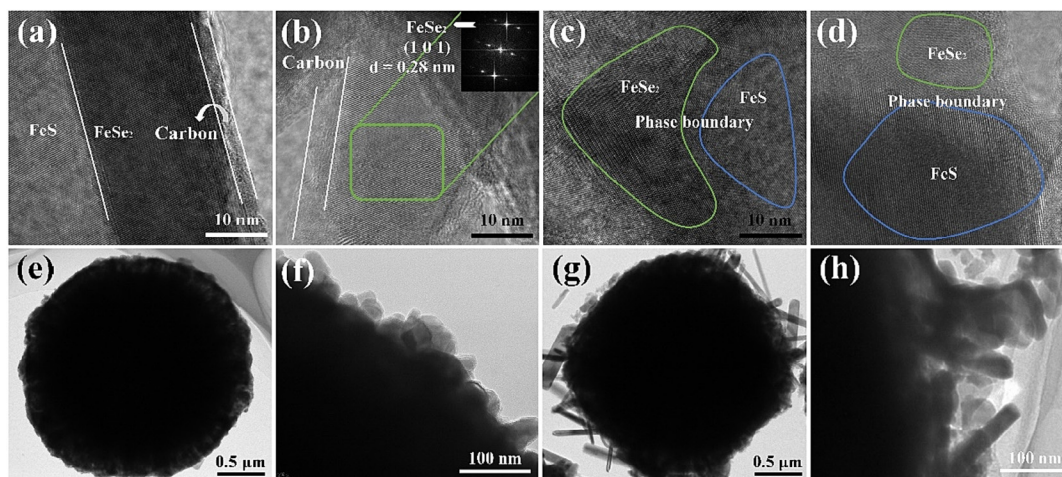


**Fig. 5.** (a–d) HRTEM images of FSSe/C-2. TEM images of (e, f) FSSe/C-1 and (g, h) FSSe/C-3.

FSSe/C-3 respectively. Insufficient selenium powder results in incomplete growth of FeSe<sub>2</sub> nanorods, which increases diffusion path and limits kinetics of Na<sup>+</sup> (Fig. 5e–f). FeSe<sub>2</sub> nanorods grow unevenly due to excess selenium, and too large nanorods are easy to break and fall off during the sodiation/desodiation, which is not beneficial for the long cycles of SIBs (Fig. 5g–h).

To test the electrochemical performance of FSSe/C as the anode of SIBs, a series of materials were assembled in a 2032-type coin cells with a counter electrode of metallic sodium. Cycling voltammograms (CV) profiles of FSSe/C-2 at 0.4 mV·s<sup>-1</sup> are shown in Fig. 6a. Owing to the building of solid electrolyte interphase (SEI) film, a significant peak at 1.18 V appears in the CV profile at first

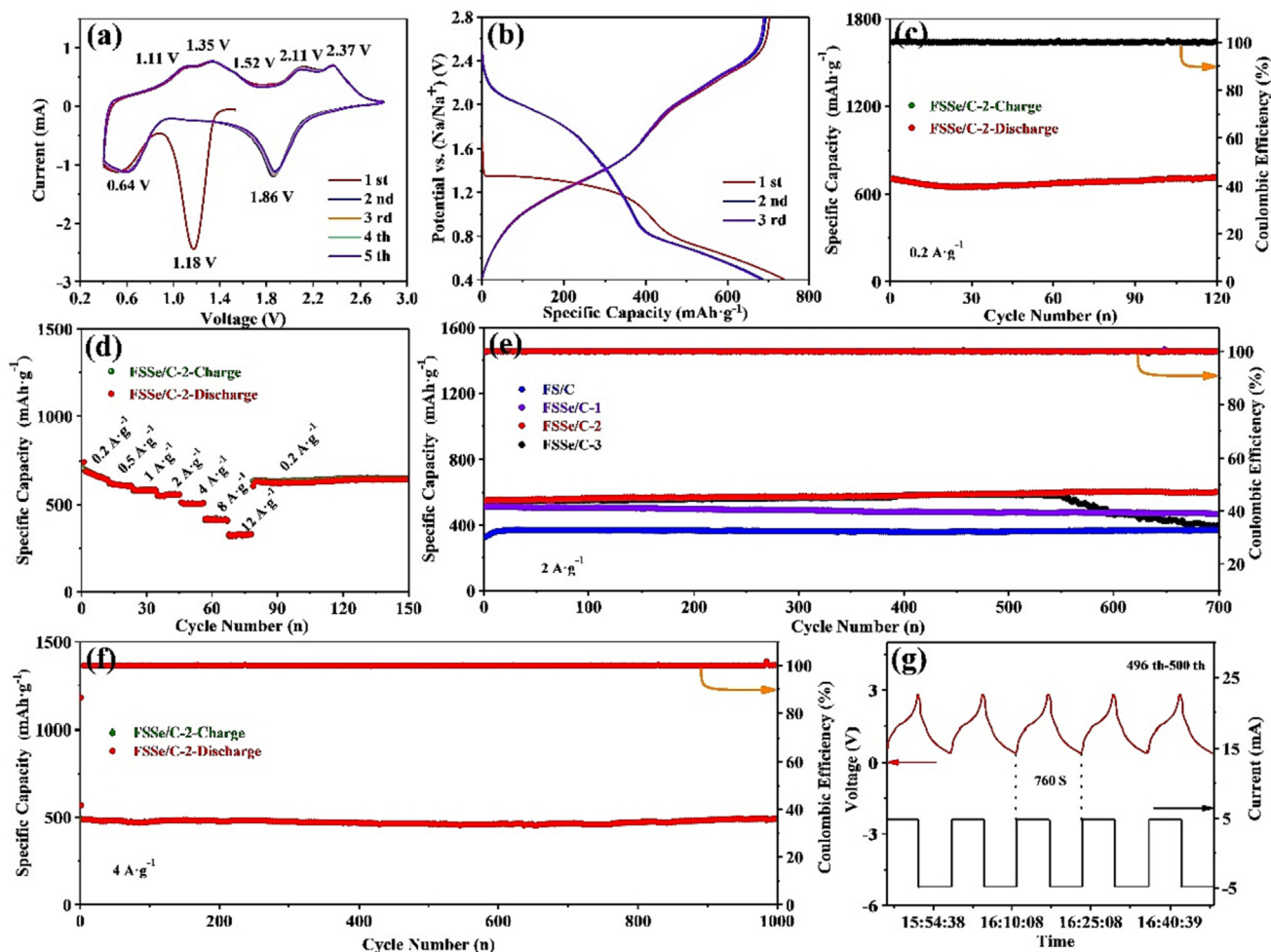


**Fig. 6.** (a) Cycling voltammograms profiles of FSSe/C-2 at  $0.4 \text{ mV s}^{-1}$ . (b) Galvanostatic charge–discharge curves at the initial 3 cycles and (c) cyclic performance of FSSe/C-2 at  $0.2 \text{ A g}^{-1}$ . (d) Rate performances at different current densities from  $0.2$  to  $12 \text{ A g}^{-1}$ . (e) Comparison of cyclic performances of FS/C, FSSe/C-1, FSSe/C-2, and FSSe/C-3 at  $2 \text{ A g}^{-1}$ . (f) Long-cyclic capability of FSSe/C-2 at  $4 \text{ A g}^{-1}$ . (g) Relationship between time and voltage&current of FSSe/C-2 at  $4 \text{ A g}^{-1}$ .

cycle. From the CV profiles at the second to fifth cycles, the nearly coincident curves indicate that the redox reaction of FSSe/C-2 is highly reversible during the charge/discharge.

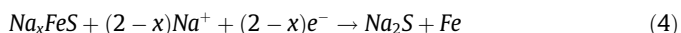
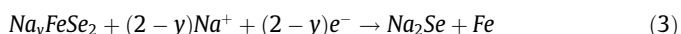
Galvanostatic charge/discharge curves at the initial 3 cycles are shown in Fig. 6b. FSSe/C-2 delivers initial Coulombic efficiency (ICE) of 94.8 % (initial discharge and charge capacity of  $742.4$  and  $703.4 \text{ mAh g}^{-1}$ , respectively) at a current density of  $0.2 \text{ A g}^{-1}$ . The Coulombic efficiency (CE) of the second cycle rises rapidly to 100 %, and the CE of the subsequent cycles maintains to 100 %. The high and stable CE demonstrates the highly reversibility of the electrochemical reaction, originating from appropriate hierarchical architecture, suitable voltage window and protection of the thin NC. After 120 cycles, FSSe/C-2 maintains reversible capacity of  $704.5 \text{ mAh g}^{-1}$  with  $0.0017 \%$  attenuation rate per cycle (Fig. 6c). The rate capability of FSSe/C-2 at different current densities from  $0.2$  to  $12 \text{ A g}^{-1}$  depicts in Fig. 6d. The average capacities of FSSe/C-2 electrode are  $670.5$ ,  $611.4$ ,  $581.5$ ,  $555.1$ ,  $505.5$ ,  $412.5$  and  $326.3 \text{ mAh g}^{-1}$  at  $0.2$ ,  $0.5$ ,  $1$ ,  $2$ ,  $4$ ,  $8$  and  $12 \text{ A g}^{-1}$ , respectively. When the current density returns to  $0.2 \text{ A g}^{-1}$ , the average capacity restores to  $635.7 \text{ mAh g}^{-1}$  with recovery rate of  $94.8 \%$  and remarkably superior to that of FS/C, suggesting that the  $\text{FeSe}_2$  nanorods grow on the outer layer of FS/C enhances the storage capacity of  $\text{Na}^+$ . The comparison of cyclic capability of FS/C, FSSe/C-1, FSSe/C-2 and FSSe/C-3 at  $2 \text{ A g}^{-1}$  are shown in Fig. 6e. After 700 cycles at  $2 \text{ A g}^{-1}$ , FSSe/C-2 delivers reversible capacity of  $601.2 \text{ mAh g}^{-1}$ ,

much higher than that of FS/C ( $370.6 \text{ mAh g}^{-1}$ ), FSSe/C-1 ( $468.1 \text{ mAh g}^{-1}$ ) and FSSe/C-3 ( $390 \text{ mAh g}^{-1}$ ). Specifically, FSSe/C-1 has higher capacity than FS/C, but its attenuated trend is obvious ( $0.0118 \%$  attenuation rate per cycle). FSSe/C-3 shows a dramatic decline in capacity after 550 cycles. To explore the reasons for the different cyclic performances, SEM and TEM images of the FSSe/C-1, FSSe/C-2 and FSSe/C-3 were investigated. After 200 cycles at  $4 \text{ A g}^{-1}$ , the spherical structure of FSSe/C-2 is in good condition and the  $\text{FeSe}_2$  rods are not damaged (Fig. S4d, S4e, S5b and S5e). And the structure keeps perfectly even after 1000 cycles, suggesting its excellent stability (Fig. S4f). Unlike FSSe/C-2, the particles in FSSe/C-1 are accumulated after 200 and 1000 cycles, leading to decay of capacity (Fig. S4a–c, S5a and S5d). The sudden and violent attenuation of the FSSe/C-3 may be the breakage of the spherical structure (Fig. S4g–i, S5c and S5f). To further explore the sodium storage capacity of FSSe/C-2, the long cyclic performance at high current density is tested and shown in Fig. 6f. FSSe/C-2 delivers initial ICE  $86.5 \%$  (discharge and charge capacity of  $567.9$  and  $491.3 \text{ mAh g}^{-1}$ , respectively) at a current density of  $4 \text{ A g}^{-1}$ . It is worth mention that the capacity of 2nd ( $492.3 \text{ mAh g}^{-1}$ ) and 1000th ( $492.2 \text{ mAh g}^{-1}$ ) cycle remains unchanged. The relationship between time and voltage&current of FSSe/C-2 at  $4 \text{ A g}^{-1}$  is depicted in Fig. 6g, which delivers that it only takes  $760 \text{ s}$  to run a charge/discharge cycle and  $380 \text{ s}$  to charge full. The excellent cycling stability and high capacity demonstrate that the synergistic

effect and hierarchical structure can effectively improve the electrochemical properties of monomeric sulfide.

CV curves were tested for different voltage ranges to analyze redox reactions. There are multiple redox peaks in CV curve of FSSe/C at 0.1–2.8 V (Fig. 7a). The peaks at 1.88, 0.43, 1.01, 1.18 and 1.31 V correspond to the redox reaction of FeS [16,47]. In particular, the reduced peak appears at 1.88 V corresponding to insertion of Na<sup>+</sup> into FeS to form Na<sub>x</sub>FeS. The subsequent peak at 0.43 V comes from the conversion of Na<sub>x</sub>FeS to Fe. The appearance of the peak at 1.01 V during the anodic process is attributed to the oxidation of Fe to Na<sub>x</sub>FeS. And two oxidation peaks at 1.18 and 1.31 V originated from desodiation of Na<sub>x</sub>FeS. When it comes to the redox reactions of FeSe<sub>2</sub>, the reduction peaks at 1.88 and 0.59 V can be attributed to Na<sub>y</sub>FeSe<sub>2</sub> and Fe [48]. The other three oxidation peaks correspond to the reverse reactions of desodiation [49,50].

Reaction equation:



The conversion reaction can increase the electrode capacity, but sodiation/desodiation reactions will lead to more structural damage than the simple intercalation reaction [22]. The conversion reactions of FeS and FeSe<sub>2</sub> occur below 0.4 V and 0.6 V, respectively. The conversion reactions of FeS and FeSe<sub>2</sub> can be controlled by adjusting the cut-off voltage to 0.4 V. FSSe/C-2 has very poor cyclic stability between voltage ranges of 0.1–2.8 V, which proves the above viewpoint (Fig. S3c). The CV curve of FSSe/C-2 at 0.4–2.8 V is depicted in Fig. 7b. The conversion peak of FeS (0.43 V) is gone and that of FeSe<sub>2</sub> (0.59 V) is weakened, proving that it is effective to control the conversion reaction by adjusting the volt-

age window. The excellent cycling stability of FSSe/C-2 is due to the control of the conversion reaction and rational structural design. After the selenation, specific surface area increases from 7.86 to 38.77 m<sup>2</sup>·g<sup>-1</sup> (Fig. 7c). A larger specific surface area improves the contact area between electrolyte and electrode, which provides more active sites for Na<sup>+</sup> and enhances the electrochemical activity.

Electrochemical impedance spectroscopy (EIS) was tested to investigate reaction kinetics of Na<sup>+</sup>. EIS plots of FS/C, FSSe/C-1, FSSe/C-2 and FSSe/C-3 are shown in Fig. 7d and the fitting dates can be found in Table S1. After growing FeSe<sub>2</sub> on the surface of FeS, the values of R<sub>ct</sub> of FSSe/C-1 (R<sub>ct</sub> = 11.44 Ω), FSSe/C-2 (R<sub>ct</sub> = 2.33 Ω) and FSSe/C-3 (R<sub>ct</sub> = 5.51 Ω) are reduced to varying degrees (FS/C, R<sub>ct</sub> = 43.18 Ω). Lattice imperfections derived from phase boundaries between FeS and FeSe<sub>2</sub> provide abundant reactive sites for sodium ion storage and enhance the electron/ion transfer capability. Among the compounds of the same composition with different proportions, FSSe/C-2 has the lowest resistance. Therefore, a proper compound ratio and homogeneous morphology are beneficial to rapid transfer of charge.

The galvanostatic intermittent titration technique (GITT) tests was employed to calculate the Na<sup>+</sup> diffusion coefficients (D<sub>Na</sub><sup>+</sup>) [51]. GITT and D<sub>Na</sub><sup>+</sup> results of FS/C and FSSe/C-2 are shown in Fig. 7e-f. FSSe/C-2 has a much higher Na<sup>+</sup> diffusion kinetics than FS/C during charging and discharging, suggesting that the hierarchical architecture of FeS, FeSe<sub>2</sub> and NC effectively enhances Na<sup>+</sup> diffusion kinetics. After the formation of SEI (Fig. 7g-h), D<sub>Na</sub><sup>+</sup> values of FSSe/C-2 show a greater increase than that of FS/C, suggesting that FSSe/C-2 has better SEI film than FS/C.

To explore the mechanism of the excellent rate capability, the electrochemical kinetics of FSSe/C-2 were studied by CV profiles. CV profiles with four main peaks (peak 1–4) at different scan rates between 0.4 and 1.4 mV·s<sup>-1</sup> are displayed in Fig. 7i. The charge storage mechanism of FSSe/C-2 can be determined by the following formula: [2,8,11]

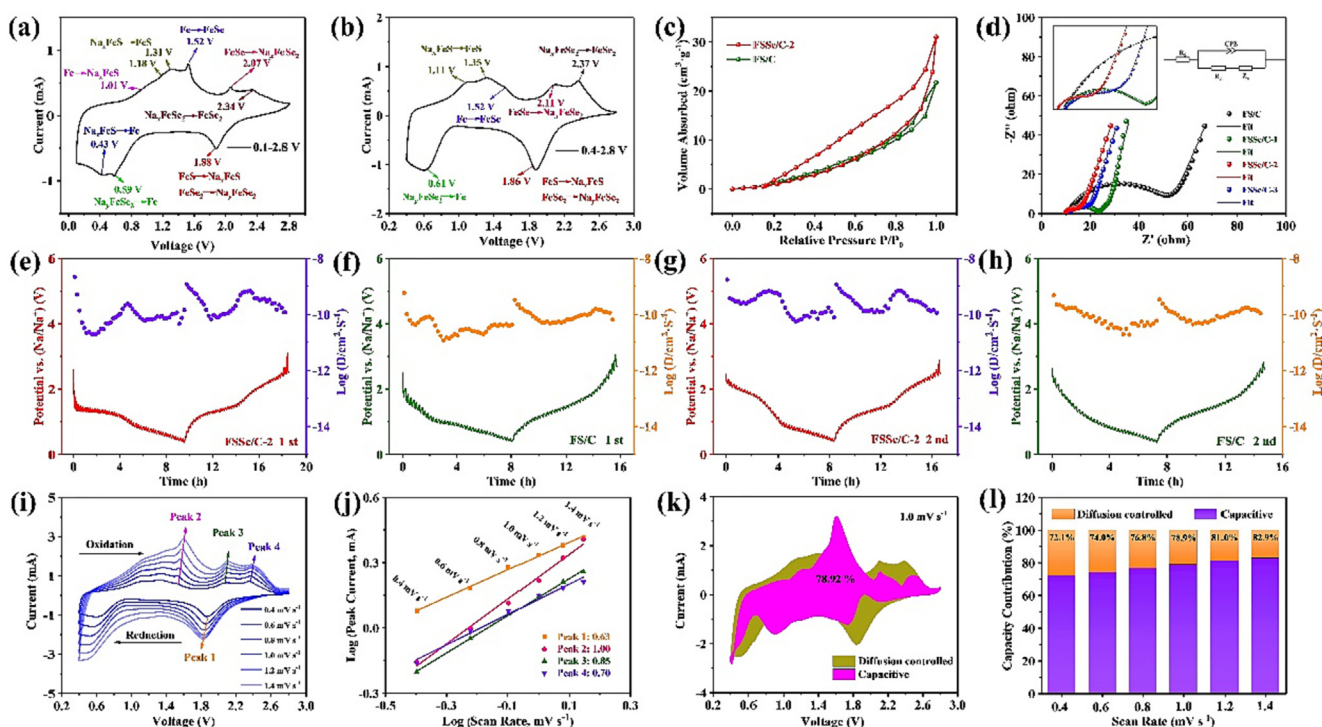


Fig. 7. Cycling voltammograms profiles of FSSe/C-2 at 0.4 mV·s<sup>-1</sup> between (a) 0.1–2.8 V and (b) 0.4–2.8 V. (c) BET surface area of FS/C and FSSe/C-2. (d) EIS plots of FS/C, FSSe/C-1, FSSe/C-2 and FSSe/C-3 before cycles. GITT test and Na<sup>+</sup> diffusion coefficients of (e, g) FSSe/C-2 and (f, h) FS/C.

$$i = av^b \quad (5)$$

$$\log(i) = b\log(v) + \log(a) \quad (6)$$

In this equation,  $i$  and  $v$  represent peak current and scan rate, respectively. The  $b$ -value, which depends on the linear relationship between  $\log(i)$  and  $\log(v)$ , can judge the charge storage mechanism [52]. Particularly, when  $b$ -value is more inclined to 0.5 or 1, the sodium storage mechanism is more inclined to diffusion-controlled process or capacitive-controlled process, respectively. The  $b$ -values of peak 1, 2, 3 and 4 are 0.63, 1.0, 0.85 and 0.7 respectively, suggesting that  $\text{Na}^+$  storage in FSSe/C-2 is mainly controlled by capacitive-controlled process (Fig. 7j). Formula 3 was taken to further analyze the contribution ratio of diffusion-controlled process to capacitive-controlled process: [53]

$$i(v) = k_1v + k_2v^{1/2} \quad (7)$$

where  $k_1v$  and  $k_2v^{1/2}$  stand for capacitive-controlled and diffusion-controlled process, respectively. After calculation, the capacitance contribution ratio at scan rates between 0.4 and 1.4  $\text{mV}\cdot\text{s}^{-1}$  are exhibited in Fig. 7l. When they = 0.4  $\text{mV}\cdot\text{s}^{-1}$ , the contribution ratio of capacitive-controlled process reaches 72.1%. As the scan rate increases to 1.4  $\text{mV}\cdot\text{s}^{-1}$ , the ratio reaches 82.9%. The high and increasing capacitive ratios demonstrate that electrochemical reactions tend to occur at the surface rather than inside the material. More surface reactions lead to faster charge transfer and better rate capability, induced by the hierarchical architecture of FSSe/C-2.

To further explore the ability of FSSe/C as a SIBs anode,  $\text{Na}_3\text{V}_2(\text{PO}_4)_3/\text{C}$  (NVP/C) as a matching cathode material was assembled with FSSe/C into the full battery. As shown in Fig. 8a, NVP/C particles with size of 150 nm were synthesized by solvothermal and annealing process, which exhibits  $76.2 \text{ mAh}\cdot\text{g}^{-1}$  at  $1 \text{ A}\cdot\text{g}^{-1}$  after 500 cycles. Fig. 8b displays a structural model diagram of NVP/C-FSSe/C full battery, where Al and Cu foil are employed as the collectors of NVP/C cathode and FSSe/C anode, respectively. Cyclic performance of NVP/C-FSSe/C full battery is exhibited in Fig. 8c, delivering reversible capacity of  $252.1 \text{ mAh}\cdot\text{g}^{-1}$  after 300 cycles at  $1 \text{ A}\cdot\text{g}^{-1}$  with 2:1 cathode and anode loading mass ratio. The excellent cyclic performance is due to the stability of cathode and anode, as well as the matching of NVP/C cathode and FSSe/C anode. Galvanostatic charge–discharge curves for NVP/C-FSSe/C full battery are depicted in Fig. 8d. The calculation result indicates that the average discharge voltage of 30th cycle is 1.74 V and energy density of NVP/C-FSSe/C full battery at  $1 \text{ A}\cdot\text{g}^{-1}$  is  $123.5 \text{ Wh}\cdot\text{kg}^{-1}$  (based on the sum of the mass of cathode and anode). The excellent cycling stability and high energy density confirm the potential of FSSe/C as an electrode for SIBs.

To describe the strength of the interface, the interface binding energy was calculated, which is defined as:

$$E_{\text{binding}} = (E_{\text{interface}} - E_{\text{part1}} - E_{\text{part2}}) / A_{\text{interface}} \quad (8)$$

where  $E_{\text{interface}}$ ,  $E_{\text{part1}}$  and  $E_{\text{part2}}$  represent the total energy of interface structure and two component surfaces, and  $A_{\text{interface}}$  represents the interface area. The calculated FeS/FeSe<sub>2</sub> interface binding energy is  $-23 \text{ meV}/\text{\AA}^2$ , delivering stronger thermal stability referring to

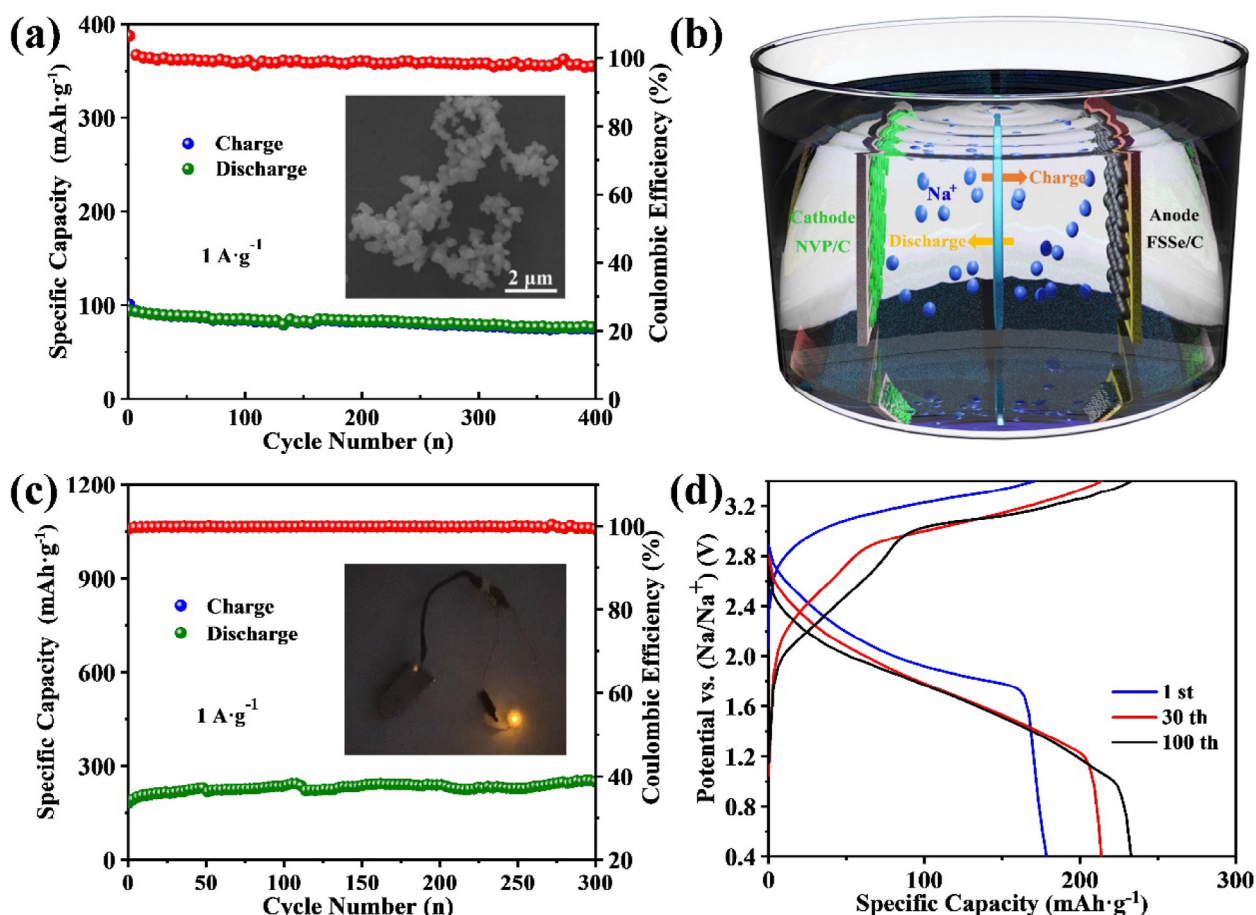


Fig. 8. (a) Cyclic performance of NVP/C at  $1 \text{ A}\cdot\text{g}^{-1}$  (illustration for its SEM image). (b) Model diagram and (c) cyclic performance (illustration for LED working) of NVP/C-FSSe/C full battery. (d) Galvanostatic charge–discharge curves of NVP/C-FSSe/C full battery.

the previous research work [54]. The adsorption energy of single  $\text{Na}^+$  was also investigated according to the following definition:

$$E_{\text{adsorption}} = (E_{\text{total}} - E_{\text{substrate}} - E_{\text{Na}}) \quad (9)$$

where  $E_{\text{total}}$ ,  $E_{\text{substrate}}$  and  $E_{\text{Na}}$  is the system adsorbed with  $\text{Na}^+$ , the interface or surface without  $\text{Na}^+$  and isolated  $\text{Na}^+$  energy, respectively.

The adsorption models of  $\text{Na}^+$  on the FeS (001),  $\text{FeSe}_2$  (001) surface and the interface are formed in Fig. 9a–c. All these configurations do not induce large lattice deformation and have the negative adsorption energies, which implies that  $\text{Na}^+$  could adsorb on these surface or interface stably. In addition, for a single  $\text{Na}^+$ , the adsorption energy ( $-3.6$  eV) on the FeS/FeSe<sub>2</sub> interface is lower than that on the FeS ( $-2.7$  eV) and FeSe<sub>2</sub> ( $-3.0$  eV) surfaces, indicating that the formation of the interface improves the adsorption capacity of  $\text{Na}^+$ .

For diffusion energy barrier calculation, as shown in Fig. 9d–e, the migration energy barrier in the bulk FeS and FeSe<sub>2</sub> are 1.43 and 1.06 eV, respectively, which is much larger than the other literature [54,55]. This is apparent because of the different interaction environments in these configurations. For bulk FeS and FeSe<sub>2</sub> crystal structures, the strong Fe–S and Fe–Se covalent bonds would prevent the migration of  $\text{Na}^+$  in the diffusion pathway. The formation of the interface provides an extra channel for the rapid migration of  $\text{Na}^+$ . Therefore, the rate performance and capacity of FSSe/C can be further enhanced.

#### 4. Conclusion

To sum up, FeS–FeSe<sub>2</sub>/NC (FSSe/C) with hierarchical architecture was obtained by hydrothermal method, carbonization and in-situ selenylation. Phase boundaries (FeS/FeSe<sub>2</sub>) induced by rationally structural design provide more  $\text{Na}^+$  active sites and extra ion channels, which improves the capacity and rate performance for sodium ion battery (SIBs). The synergistic effect of FeS and FeSe<sub>2</sub> effectively enhances the electrochemical activity and decreases the diffusion resistance, which contributes to transfer kinetics of  $\text{Na}^+$ . The stability of FSSe/C is further enhanced by controlling the conversion reaction. The density functional theory (DFT) calculation also proves that the interfaces of FeS/FeSe<sub>2</sub> can provide the adsorption site and reduce the adsorption energy of  $\text{Na}^+$ . As a result, FSSe/C anode delivers high reversible capacity (704.5  $\text{mAh}\cdot\text{g}^{-1}$  after 120 cycles at  $0.2$   $\text{A}\cdot\text{g}^{-1}$ ), excellent rate performance (326.3  $\text{mAh}\cdot\text{g}^{-1}$  at  $12$   $\text{A}\cdot\text{g}^{-1}$ ), and outstanding stability (492.3  $\text{mAh}\cdot\text{g}^{-1}$  after 1000 cycles at  $4$   $\text{A}\cdot\text{g}^{-1}$ ). In terms of cyclic and rate performance, FSSe/C shows a competitive advantage over other recent sulfides or selenides [4,56–61]. Moreover, a full battery pairing FSSe/C anode with  $\text{Na}_3\text{V}_2(\text{PO}_4)_3/\text{C}$  (NVP/C) cathode has been fabricated, exhibiting high reversible capacity ( $252.1$   $\text{mAh}\cdot\text{g}^{-1}$  after 300 cycles at  $1$   $\text{A}\cdot\text{g}^{-1}$ ) and superior energy density ( $123.5$   $\text{Wh}\cdot\text{kg}^{-1}$ ). Consequently, this work provides a new perspective on bonding iron chalcogenides in a hierarchical structure for high-stability sodium storage.

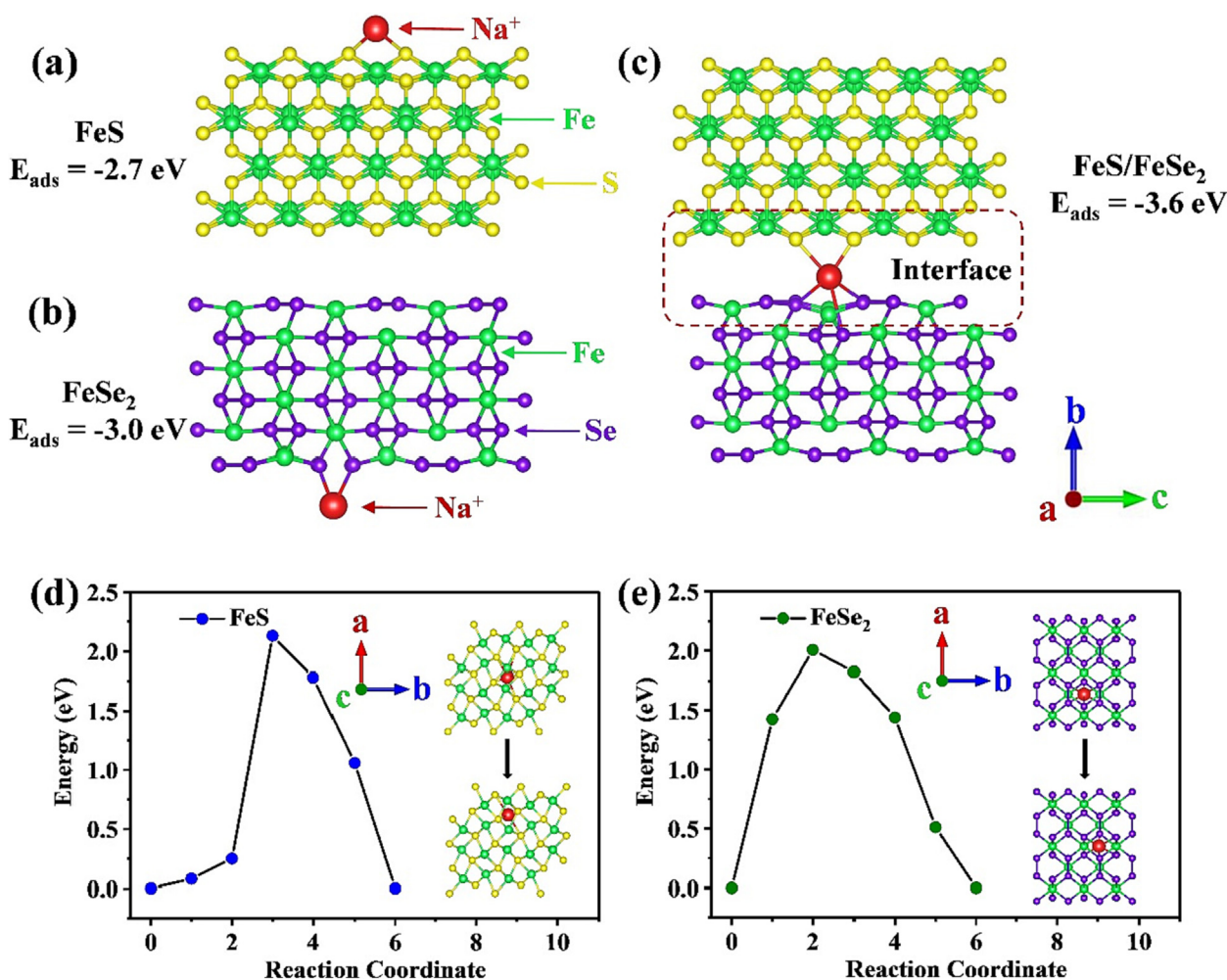


Fig. 9. The adsorption models of  $\text{Na}^+$  on the (a) FeS surface, (b) FeSe<sub>2</sub> surface and (c) FeS/FeSe<sub>2</sub> interface. Equivalent crystal lattice positions of  $\text{Na}^+$  diffusion path in (d) FeS and (e) FeSe<sub>2</sub>.

## CRediT authorship contribution statement

**Hongyi Chen:** Resources, Software, Investigation, Visualization, Conceptualization, Data curation, Formal analysis, Methodology, Writing - original draft, Writing - review & editing. **Pengfei Lv:** Data curation, Visualization, Software. **Qiming Liu:** Data curation. **Pengfu Tian:** Visualization. **Shiyue Cao:** Data curation, Validation. **Shengjun Yuan:** Data curation, Visualization.

## Data availability

The data that has been used is confidential.

## Declaration of Competing Interest

The authors declare that they have no known competing financial interests or personal relationships that could have appeared to influence the work reported in this paper.

## Acknowledgments

This work was financial supported by the National Natural Science Foundation of China (51572202) and Duozhu Technology (Wuhan) Co., LTD. We thank Dr. Xiaodong Zhou from the Core Facility of Wuhan University for his help with SEM analysis.

## Appendix A. Supplementary material

Supplementary data to this article can be found online at <https://doi.org/10.1016/j.jcis.2023.01.056>.

## References

- J. Liu, Y.G. Xu, L.B. Kong, Synthesis of polyvalent ion reaction of MoS<sub>2</sub>/CoS<sub>2</sub>-RGO anode materials for high-performance sodium-ion batteries and sodium-ion capacitors, *J. Colloid Interface Sci.* 575 (2020) 42–53.
- L. Cao, X. Gao, B. Zhang, X. Ou, J. Zhang, W.-B. Luo, Bimetallic Sulfide Sb<sub>2</sub>S<sub>3</sub>@FeS<sub>2</sub> Hollow Nanorods as High-Performance Anode Materials for Sodium-Ion Batteries, *ACS Nano* 14 (2020) 3610–3620.
- S.S. Shi, C.L. Sun, X.P. Yin, L.Y. Shen, Q.H. Shi, K.N. Zhao, Y.F. Zhao, J.J. Zhang, FeP Quantum Dots Confined in Carbon-Nanotube-Grafted P-Doped Carbon Octahedra for High-Rate Sodium Storage and Full-Cell Applications, *Adv. Funct. Mater.* 30 (2020).
- L.K. Fu, W.Q. Xiong, Q.M. Liu, S.Y. Wan, C.X. Kang, G.F. Li, J. Chu, Y.C. Chen, S.J. Yuan, Metal-organic framework derived FeS/MoS<sub>2</sub> composite as a high performance anode for sodium-ion batteries, *J. Alloy. Compd.* 869 (2021).
- B.B. Wang, S.P. Zhang, G. Wang, H. Wang, J.T. Bai, The morphology and electrochemical properties of porous Fe<sub>2</sub>O<sub>3</sub>@C and FeS@C nanofibers as stable and high-capacity anodes for lithium and sodium storage, *J. Colloid Interface Sci.* 557 (2019) 216–226.
- S.Y. Wan, X. Liu, L.K. Fu, C.B. Zhou, H.Y. Chen, G.H. Li, S.Y. Cao, Q.M. Liu, Hierarchical self-assembled SnS@N-S dual-doped carbon microflower spheres as anode for high performance lithium-ion batteries, *J. Alloy. Compd.* 870 (2021).
- L.B. Fang, Z.Y. Lan, W.H. Guan, P. Zhou, N. Bahlawane, W.P. Sun, Y.H. Lu, C. Liang, M. Yan, Y.Z. Jiang, Hetero-interface constructs ion reservoir to enhance conversion reaction kinetics for sodium/lithium storage, *Energy Storage Mater.* 18 (2019) 107–113.
- L.T. Liu, X.Y. Sun, Y. Dong, D.K. Wang, Z. Wang, Z.J. Jiang, A. Li, X.H. Chen, H.H. Song, N-doped hierarchical porous hollow carbon spheres with multi-cavities for high performance Na-ion storage, *J. Power Sources* 506 (2021).
- D. Cao, W. Kang, W. Wang, K. Sun, Y. Wang, P. Ma, D. Sun, Okra-Like Fe<sub>7</sub>S<sub>8</sub>/C@ZnS/N-C@C with Core-Double-Shelled Structures as Robust and High-Rate Sodium Anode, *Small* 16 (2020).
- K. Zhang, M. Park, L. Zhou, G.-H. Lee, J. Shin, Z. Hu, S.-L. Chou, J. Chen, Y.-M. Kang, Cobalt-Doped FeS<sub>2</sub> Nanospheres with Complete Solid Solubility as a High-Performance Anode Material for Sodium-Ion Batteries, *Angewandte Chem.-Int. Ed.* 55 (2016) 12822–12826.
- W. Yan, M. Cao, S. Fan, X. Liu, T. Liu, H. Li, J. Su, Multi-yolk ZnSe<sub>2</sub>/(CoSe<sub>2</sub>)@NC heterostructures confined in N-doped carbon shell for high-efficient sodium-ion storage, *Compos. Part B-Eng.* 213 (2021).
- Y.Y. Zhou, K. Jiang, Z.G. Zhao, Q.W. Li, R.Z. Ma, T. Sasaki, F.X. Geng, Giant two-dimensional titania sheets for constructing a flexible fiber sodium-ion battery with long-term cycling stability, *Energy Storage Mater.* 24 (2020) 504–511.
- S.G. Zhang, J. Mi, H.P. Zhao, W.Y. Ma, L.Y. Dang, L.C. Yue, Electrospun N-doped carbon nanofibers confined Fe<sub>1-x</sub>S composite as superior anode material for sodium-ion battery, *J. Alloy. Compd.* 842 (2020).
- X. Li, T. Liu, Y.X. Wang, S.L. Chou, X. Xu, A.M. Cao, L.B. Chen, S/N-doped carbon nanofibers affording Fe<sub>7</sub>S<sub>8</sub> particles with superior sodium storage, *J. Power Sources* 451 (2020).
- Z. Ali, M. Asif, X. Huang, T. Tang, Y. Hou, Hierarchically Porous Fe<sub>2</sub>CoSe<sub>4</sub> Binary-Metal Selenide for Extraordinary Rate Performance and Durable Anode of Sodium-Ion Batteries, *Adv. Mater.* 30 (2018).
- S.Z. Huang, Y. Li, S. Chen, Y. Wang, Z.H. Wang, S. Fan, D.H. Zhang, H.Y. Yang, Regulating the breathing of mesoporous Fe<sub>0.95</sub>S<sub>1.05</sub> nanorods for fast and durable sodium storage, *Energy Storage Mater.* 32 (2020) 151–158.
- H. Liu, C. Lv, S. Chen, X. Song, B. Liu, J. Sun, H. Zhang, D. Yang, X. She, X. Zhao, Fe-alginate biomass-derived FeS/3D interconnected carbon nanofiber aerogels as anodes for high performance sodium-ion batteries, *J. Alloy. Compd.* 795 (2019) 54–59.
- A.K. Haridas, J. Heo, X. Li, H.-J. Ahn, X. Zhao, Z. Deng, M. Agostini, A. Matic, J.-H. Ahn, A flexible and free-standing FeS/sulfurized polyacrylonitrile hybrid anode material for high-rate sodium-ion storage, *Chem. Eng. J.* 385 (2020).
- X. Zhang, X. Gao, J. Li, K. Hong, L. Wu, S. Xu, K. Zhang, C. Liu, Z. Rao, In-situ synthesis of Fe<sub>7</sub>S<sub>8</sub> nanocrystals decorated on N, S-codoped carbon nanotubes as anode material for high-performance lithium-ion batteries, *J. Colloid Interface Sci.* 579 (2020) 699–706.
- J.H. Chu, Q.Y. Yu, K. Han, L.D. Xing, C. Gu, Y. Li, Y.P. Bao, W. Wang, Yolk-shell structured FeS/MoS<sub>2</sub>@nitrogen-doped carbon nanocubes with sufficient internal void space as an ultrastable anode for potassium-ion batteries, *J. Mater. Chem. A* 8 (2020) 23983–23993.
- D.Y. Gui, Z.J. Wei, J. Chen, L.W. Yan, J. Li, P.X. Zhang, C.Y. Zhao, Boosting the sodium storage of the 1T/2H MoS<sub>2</sub>@SnO<sub>2</sub> heterostructure via a fast surface redox reaction, *J. Mater. Chem. A* 9 (2021) 463–471.
- Z. Hu, Z. Zhu, F. Cheng, K. Zhang, J. Wang, C. Chen, J. Chen, Pyrite FeS<sub>2</sub> for high-rate and long-life rechargeable sodium batteries, *Energ. Environ. Sci.* 8 (2015) 1309–1316.
- P. Wang, Y. Zhang, Y. Yin, L. Fan, N. Zhang, K. Sun, In Situ Synthesis of CuCo<sub>2</sub>S<sub>4</sub>@N/S-Doped Graphene Composites with Pseudocapacitive Properties for High-Performance Lithium-Ion Batteries, *ACS Appl. Mater. Interfaces* 10 (2018) 11708–11714.
- J.H. Yang, C. Zhang, Y.D. Niu, J. Huang, X. Qian, K.Y. Wong, N-doped C-CoS<sub>2</sub>@CoS<sub>2</sub>/MoS<sub>2</sub> nano polyhedrons with hierarchical yolk-shelled structures as bifunctional catalysts for enhanced photovoltaics and hydrogen evolution, *Chem. Eng. J.* 409 (2021).
- Z. Lu, Y. Zhai, N. Wang, Y. Zhang, P. Xue, M. Guo, B. Tang, D. Huang, W. Wang, Z. Bai, S. Dou, FeS<sub>2</sub> nanoparticles embedded in N/S co-doped porous carbon fibers as anode for sodium-ion batteries, *Chem. Eng. J.* 380 (2020).
- C.H. Yang, X.H. Liang, X. Ou, Q.B. Zhang, H.S. Zheng, F.H. Zheng, J.H. Wang, K.V. Huang, M.L. Liu, Heterostructured Nanocube-Shaped Binary Sulfide (SnCo)<sub>2</sub>-S Interlaced with S-Doped Graphene as a High-Performance Anode for Advanced Na+ Batteries, *Adv. Funct. Mater.* 29 (2019).
- Y.J. Fang, D.Y. Luan, Y. Chen, S.Y. Gao, X.W. Lou, Synthesis of Copper-Substituted CoS<sub>2</sub>@CuxS Double-Shelled Nanoboxes by Sequential Ion Exchange for Efficient Sodium Storage, *Angewandte Chem.-Int. Ed.* 59 (2020) 2644–2648.
- Y. Fang, D. Luan, X.W. Lou, Recent Advances on Mixed Metal Sulfides for Advanced Sodium-Ion Batteries, *Adv. Mater.* 32 (2020).
- W.J. Yang, L.J. Han, X.J. Liu, L. Hong, M.D. Wei, Template-free fabrication of 1D core-shell MoO<sub>2</sub>@MoS<sub>2</sub>/nitrogen-doped carbon nanorods for enhanced lithium/sodium-ion storage, *J. Colloid Interface Sci.* 588 (2021) 804–812.
- S.H. Dong, C.X. Li, Z.Q. Li, L.Y. Zhang, L.W. Yin, Mesoporous Hollow Sb/ZnS@C Core-Shell Heterostructures as Anodes for High-Performance Sodium-Ion Batteries, *Small* 14 (2018).
- Z.Q. Li, L.Y. Zhang, X.L. Ge, C.X. Li, S.H. Dong, C.X. Wang, L.W. Yin, Core-shell structured CoP/FeP porous microcubes interconnected by reduced graphene oxide as high performance anodes for sodium ion batteries, *Nano Energy* 32 (2017) 494–502.
- H. Chen, P. Tian, L. Fu, S. Wan, Q.J.C.E.J. Liu, Hollow spheres of solid solution Fe<sub>7</sub>Ni<sub>3</sub>S<sub>11</sub>/CN as advanced anode materials for sodium ion batteries, 430 (2022) 132688.
- P.E. Blochl, Projector augmented-wave method, *Phys. Rev. B* 50 (1994) 17953–17979.
- G. Kresse, J. Furthmuller, Efficient iterative schemes for ab initio total-energy calculations using a plane-wave basis set, *Phys. Rev. B* 54 (1996) 11169–11186.
- D. Chakraborty, K. Berland, T. Thonhauser, Next-Generation Nonlocal van der Waals Density Functional, *J. Chem. Theory Comput.* 16 (2020) 5893–5911.
- H.J. Monkhorst, J.D.J.P.R.B. Pack, Special points for Brillouin-zone integrations, 13 (1976) 5188.
- G. Henkelman, B.P. Uberuaga, H. Jonsson, A climbing image nudged elastic band method for finding saddle points and minimum energy paths, *J. Chem. Phys.* 113 (2000) 9901–9904.
- W. Zhao, C. Guo, C.M. Li, Lychee-like FeS<sub>2</sub>@FeSe<sub>2</sub> core-shell microspheres anode in sodium ion batteries for large capacity and ultralong cycle life, *J. Mater. Chem. A* 5 (2017) 19195–19202.
- H.Y. Chen, X.T. Yang, P.F. Lv, P.F. Tian, S.Y. Wan, Q.M. Liu, Mn-doped FeS with larger lattice spacing as advance anode for sodium ion half/full battery, *Chem. Eng. J.* 450 (2022).

- [40] Y.Y. Wang, D.X. Cao, K.L. Zhang, W.P. Kang, X.T. Wang, P. Ma, Y.F. Wan, D.W. Cao, D.F. Sun, Cation-exchange construction of ZnSe/Sb(2)Se(3)hollow microspheres coated by nitrogen-doped carbon with enhanced sodium ion storage capability, *Nanoscale* 12 (2020) 17915–17924.
- [41] B.Q. Li, Y. Liu, Y.P. Li, S.H. Jiao, S.Y. Zeng, L. Shi, G.Q. Zhang, Dual-Functional Template-Directed Synthesis of MoSe<sub>2</sub>/Carbon Hybrid Nanotubes with Highly Disordered Layer Structures as Efficient Alkali-Ion Storage Anodes beyond Lithium, *ACS Appl. Mater. Interfaces* 12 (2020) 2390–2399.
- [42] Y.T. Feng, M.Z. Xu, T. He, B.J. Chen, F. Gu, L.H. Zu, R.J. Meng, J.H. Yang, CoPSe: A New Ternary Anode Material for Stable and High-Rate Sodium/Potassium-Ion Batteries, *Adv. Mater.* 33 (2021).
- [43] X.D. Ma, X.H. Xiong, P.J. Zou, W.Z. Liu, F. Wang, L.W. Liang, Y. Liu, C.Z. Yuan, Z. Lin, General and Scalable Fabrication of Core-Shell Metal Sulfides@C Anchored on 3D N-Doped Foam toward Flexible Sodium Ion Batteries, *Small* 15 (2019).
- [44] D.H. Li, Y.Y. Sun, S. Chen, J.Y. Yao, Y.H. Zhang, Y.Z. Xia, D.J. Yang, Highly Porous FeS/Carbon Fibers Derived from Fe-Carrageenan Biomass: High-capacity and Durable Anodes for Sodium-Ion Batteries, *ACS Appl. Mater. Interfaces* 10 (2018) 17175–17182.
- [45] X.J. Xu, Z.B. Liu, S.M. Ji, Z.S. Wang, Z.Y. Ni, Y.Q. Lv, J.W. Liu, J. Liu, Rational synthesis of ternary FeS@TiO<sub>2</sub>@C nanotubes as anode for superior Na-ion batteries, *Chem. Eng. J.* 359 (2019) 765–774.
- [46] Q.M. He, K. Rui, J.H. Yang, Z.Y. Wen, Fe<sub>7</sub>S<sub>8</sub> Nanoparticles Anchored on Nitrogen-Doped Graphene Nanosheets as Anode Materials for High-Performance Sodium-Ion Batteries, *ACS Appl. Mater. Interfaces* 10 (2018) 29476–29485.
- [47] S.Z. Huang, S. Fan, L.X. Xie, Q.Y. Wu, D.Z. Kong, Y. Wang, Y.V. Lim, M. Ding, Y. Shang, S. Chen, H.Y. Yang, Promoting Highly Reversible Sodium Storage of Iron Sulfide Hollow Polyhedrons via Cobalt Incorporation and Graphene Wrapping, *Adv. Energy Mater.* 9 (2019).
- [48] Q. Pan, M. Zhang, L. Zhang, Y. Li, Y. Li, C. Tan, F. Zheng, Y. Huang, H. Wang, Q. Li, FeSe<sub>2</sub>@C Microrods as a Superior Long-Life and High-Rate Anode for Sodium Ion Batteries, *ACS Nano* 14 (2020) 17683–17692.
- [49] T. Wang, W. Guo, G. Wang, H. Wang, J. Bai, B. Wang, Highly dispersed FeSe<sub>2</sub> nanoparticles in porous carbon nanofibers as advanced anodes for sodium and potassium ion batteries, *J. Alloy. Compd.* 834 (2020).
- [50] S. Jiang, M. Xiang, J. Zhang, S. Chu, A. Marcelli, W. Chu, D. Wu, B. Qian, S. Tao, L. Song, Rational design of hierarchical FeSe<sub>2</sub> encapsulated with bifunctional carbon cuboids as an advanced anode for sodium-ion batteries, *Nanoscale* 12 (2020) 22210–22216.
- [51] P. Zhou, M.Y. Zhang, L.P. Wang, Q.Z. Huang, Z.A. Su, P. Xu, R.H. Zou, X.D. Wang, C. Zeng, K.X. Ba, MOFs-Derived Flower-Like Hierarchically Porous Zn-Mn-Se/C Composite for Extraordinary Rate Performance and Durable Anode of Sodium-Ion and Potassium-Ion Batteries, *Small* 18 (2022).
- [52] J.W. Sun, S.L. Jiao, G. Lian, L.Y. Jing, D.L. Cui, Q.L. Wang, C.P. Wong, Hierarchical MoS<sub>2</sub>/m-C@a-C@Ti<sub>3</sub>C<sub>2</sub> nanohybrids as superior electrodes for enhanced sodium storage and hydrogen evolution reaction, *Chem. Eng. J.* 421 (2021).
- [53] W.X. Zhao, X.Q. Ma, Hierarchical Scalelike Yolk-Shell Construction Assembled via Ultrathin MoSe<sub>2</sub> Nanoplates Incorporated into Metal-Organic Frameworks Derived Porous Carbon Spheres as Highly Durable Anode for Enhanced Sodium Storage, *ACS Sustain. Chem. Eng.* 8 (2020) 19040–19050.
- [54] T.S. Wang, D. Legut, Y.C. Fan, J. Qin, X.F. Li, Q.F. Zhang, Building Fast Diffusion Channel by Constructing Metal Sulfide/Metal Selenide Heterostructures for High-Performance Sodium Ion Batteries Anode, *Nano Lett.* 20 (2020) 6199–6205.
- [55] S.Q. Zhang, L.L. Sun, L. Yu, G.H. Zhai, L.X. Li, X.J. Liu, H. Wang, Core-Shell CoSe<sub>2</sub>/WSe<sub>2</sub> Heterostructures@Carbon in Porous Carbon Nanosheets as Advanced Anode for Sodium Ion Batteries, *Small* 17 (2021).
- [56] S.Y. Wan, Q.M. Liu, H.Y. Chen, H.J. Zhu, Y.L. Wang, S.Y. Cao, Bimetallic sulfides SnS/FeS particles anchored on tremella-like carbon as advanced anode material for sodium ion storage, *J. Power Sources* 542 (2022).
- [57] H. Shan, J. Qin, Y.C. Ding, H.M.K. Sari, X.X. Song, W. Liu, Y.C. Hao, J.J. Wang, C. Xie, J.J. Zhang, X.F. Li, Controllable Heterojunctions with a Semicohesive Phase Boundary Boosting the Potassium Storage of CoSe<sub>2</sub>/FeSe<sub>2</sub>, *Adv. Mater.* 33 (2021).
- [58] G.K. Veerasubramani, M.S. Park, J.Y. Choi, Y.S. Lee, S.J. Kim, D.W. Kim, Rational Combination of an Alabandite MnS Laminated Pyrrhotite Fe<sub>1-x</sub>S Nanocomposite as a Superior Anode Material for High Performance Sodium-Ion Battery, *ACS Sustain. Chem. Eng.* 7 (2019) 5921–5930.
- [59] D.L. Xie, S. Cai, X.H. Sun, T.Y. Hou, K.E. Shen, R. Ling, A.R. Fan, R.Z. Zhang, S. Jiang, Y.S. Lin, FeS/ZnS nanoflower composites as high performance anode materials for sodium ion batteries, *Inorg. Chem. Commun.* 111 (2020).
- [60] J.W. Liu, S.H. Xiao, X.Y. Li, Z.Z. Li, X.R. Li, W.S. Zhang, Y. Xiang, X.B. Niu, J.S. Chen, Interface engineering of Fe<sub>3</sub>Se<sub>4</sub>/FeSe heterostructure encapsulated in electrospun carbon nanofibers for fast and robust sodium storage, *Chem. Eng. J.* 417 (2021).
- [61] J.J. Yuan, W. Liu, X.K. Zhang, Y.H. Zhang, W.T. Yang, W.D. Lai, X.K. Li, J.J. Zhang, X.F. Li, MOF derived ZnSe-FeSe<sub>2</sub>/RGO Nanocomposites with enhanced sodium/potassium storage, *J. Power Sources* 455 (2020).